**Atmospheric
Measurement
Techniques
Discussions**

Fallspeed measurement and high-resolution multi-angle photography of hydrometeors in freefall

T. J. Garrett[1], C. Fallgatter[1], K. Shkurko[1], and D. Howlett[2]

[1]Department of Atmospheric Sciences, University of Utah, Salt Lake City, Utah, USA
[2]Alta Center for Snow Science, Alta, Utah, USA

Correspondence to: T. J. Garrett (tim.garrett@utah.edu)

Discussion Paper | Discussion Paper | Discussion Paper | Discussion Paper

AMTD

5, 4827–4850, 2012

Hydrometeor fallspeed and multi-angle photography

T. J. Garrett et al.

Title Page

Abstract	Introduction
Conclusions	References
Tables	Figures

◄◄	►►
◄	►
Back	Close

Full Screen / Esc

Printer-friendly Version

Interactive Discussion

Abstract

We describe here a new instrument for imaging hydrometeors in freefall. The Multi-Angle Snowflake Camera (MASC) captures high resolution photographs of hydrometeors from three angles while simultaneously measuring their fallspeed. Based on the stereoscopic photographs captured over the two months of continuous measurements obtained at a high altitude location within the Wasatch Front in Utah, we derive statistics for fallspeed, hydrometeor size, shape, orientation and aspect ratio. From a selection of the photographed hydrometeors, an illustration is provided for how the instrument might be used for making improved microwave scattering calculations. Complex, aggregated snowflake shapes appear to be more strongly forward scattering, at the expense of reduced back-scatter, than graupel particles of similar size.

1   Introduction

Despite dramatic progress in numerical weather prediction over the past several decades, a long-standing Achilles heel of mesoscale forecasting models is their representations of precipitation microphysics (e.g. Lin et al., 1983; Rutledge and Hobbs, 1984; Reisner et al., 1998). Microphysical processes are complicated to simulate, while modeled storm lifetime and precipitation rates are exquisitely sensitive to what types of hydrometeors form, and how fast they grow and fall (Garvert et al., 2005; Colle et al., 2005; Milbrandt et al., 2010).

Hydrometeor form is also relevant for making calculations of the hydrometeor electromagnetic scattering characteristics required for remote sensing applications and microwave communications. Radar measurement is based on the intensity of back-scattering by snowflakes (e.g. Matrosov, 2007; Liu, 2008b), while radiometer measurement is based on the reduction of upwelling microwave energy that is initially emitted by surface and lower atmospheric gases, and then scattered by snowflakes in the atmosphere (e.g. Skofronick-Jackson et al., 2004; Noh et al., 2009). Radio communications

signals can be significantly depolarized by precipitation, and attenuation can range up to 3 dB per kilometer (Oguchi, 1983). Normally, however, existing databases for calculating scattering by precipitation are based on calculations for very idealized hydrometeor forms (Maruyama and Fujiyoshi, 2005; Westbrook et al., 2006; Ishimoto, 2008; Nowell, 2010).

Accurate characterization of hydrometeor shape appears to be essential for accurate representations of either of these two problems. Rimed graupel normally has a terminal fallspeed that is much higher than that of spatial aggregates, so that when graupel is diagnosed, it contributes to more rapid simulated dessication of storms (Colle et al., 2005). With respect to microwave scattering calculations, the minimum computational requirement for discrete dipole scattering calculations is a grid spacing that satisfies

$$|n|kd < 0.5 \tag{1}$$

where $|n|$ is the refractive index, k is the wavenumber ($2\pi/\lambda$) and d the dipole spacing (Draine and Flatau, 2008). So, for example, lookup tables for a high frequency 183 GHz radiometer ($\lambda = 1.6$ mm, $|n| \sim 1.78$), as anticipated for the Global Precipitation Measurement mission, would require snowflake models defined by a mesh finer than at most 72 μm.

Constraining the problem with empirical data has proved challenging. Traditionally this has been done through the painstaking manual examination of individual hydrometeors (Locatelli and Hobbs, 1974; Bruintjes et al., 1987; Mitchell et al., 1990; Thériault et al., 2012). Automated ground-based disdrometers have recently helped eliminate human subjectivity and allowed for greater statistical power (e.g. Kruger and Krajewski, 2002; Barthazy et al., 2004; Yuter et al., 2006; Newman et al., 2009; Zawadzki et al., 2010). Nonetheless, these newer instruments require imaging small, complex, fast-moving particles on a laser diode optical array, and this can lead to significant sizing errors (Yuter et al., 2006). Further, the images are normally silhouettes with a very coarse resolution of about 200 μm, which makes it very difficult to confidently discriminate particle habit (Barthazy and Schefold, 2006). It is impossible to assess the extent

of riming from 40 µm diameter droplets within silhouetted images at 200 µm resolution, or to easily discriminate them from tight clumps of aggregates.

What is needed is a measurement technique that provides automated high resolution images of hydrometeors in freefall, while simultaneously measuring their fall speed. This paper describes a new instrument with these capabilities, and summarizes a few of the statistical properties of hundreds of thousands of hydrometeors sampled during the winter of early 2012. The article concludes with an illustration of how the instrument might be used to refine microwave scattering calculations by hydrometeors.

2   The Multi-Angle Snowflake Camera

The Multi-Angle Snowflake Camera, or MASC, was developed to address the need for high-resolution multi-angle imaging of hydrometeors in freefall, while simultaneously measuring their fallspeed. The instrument was developed out of the University of Utah and is now available through Fallgatter Technologies.

As illustrated in the schematic drawing in Fig. 1, the MASC consists of three cameras, separated by 36° and each pointing at an identical focal point approximately 10 cm away. The focal point itself lies within a ring through which hydrometeors fall. The ring houses a system of near-infrared emitter-detector pairs, arranged in two arrays that are separated vertically by 32 mm. Hydrometeors passing through the lower array simultaneously trigger each of the three cameras as well as a bank of lights aimed at the center of the camera depth of field. Fall speed is calculated from the time it takes to traverse the distance between the upper and lower triggering array.

The cameras and lenses are commercially available. The MASC described here was deployed with two Unibrain Fire-i 785b (grayscale) 1280 × 960 pixel cameras in the outer positions, and one Unibrain Fire-i 980b (grayscale) 2456 × 2058 pixel camera in the center position. The lower resolution cameras used either 12 mm Pentax or 16 mm Fujinon Megapixel C-mount lenses. The higher resolution camera was fitted with a Navitar Megapixel C-mount lens.

Table 1 summarizes the camera parameters, along with their respective values for depth of field and image resolution as determined using a calibration target. Shorter lenses have the disadvantage of lower resolution, but the advantage of a larger depth of field and horizontal field of view. Conversely, the 35 mm lens begins to approximate the 9 cm object distance. This "macro" perspective constrains the depth of field with the advantage that the pixel resolution is just 9 µm. While it might seem that a 16 mm lens on a 5 MP camera body would offer the optimal mix of high resolution and a large depth of field, this is not in fact the case. Rather, for a fixed lens and digital sensor size, swapping a 1.2 MP body with a 5 MP body merely doubles the field of view while maintaining a constant image resolution in µm units.

The camera exposure time required to capture fine details in falling hydrometeors at close range is extremely short. For the results described here, 1/25 000th of a second was chosen. This speed is sufficiently fast to capture a vertical resolution of 40 µm in a hydrometeor falling at $1 \, \text{m s}^{-1}$ while allowing for adequate light from the MASC's three 2700 lumen light emitting diodes. LEDs were chosen over a traditional xenon flash system because they require much lower voltages, are longer lived, and are technically easier to implement where images might be collected at a rate of once per second, in cold conditions, and continuously over long periods. Upgrades are underway to enable higher powered and more concentrated light, with the expectation that it will allow for shorter exposure times and larger depths of field.

The infrared motion sensor device that is used for triggering the cameras and measuring fallspeed has been designed to detect the smallest hydrometeors. Each sensor array contains two near-infrared emitter/detector pairs, with an intersection point that spans the horizontal domain occupied by the camera depth of field. Each emitter/detector pair is based on a set of four near-infrared LEDs facing four opposite photodiodes. Each emitter subtends a 6° angle and each photodiode a 15° viewing angle. The intersection point of the two pairs is highlighted in Fig. 1, and occupies a maximum cross-section of $3100 \, \text{mm}^2$.

With this setup, a 10 mm camera depth of field corresponds to just 2.5 % of the trigger depth of field. Thus, a large number of camera images are triggered when the hydrometeor is at least partly outside the camera depth of field. As shown in Fig. 1, one option for reducing this inconsistency is to physically block part of the lower emitter array. For example, if the two outermost emitters are blocked then the trigger depth of field is reduced to 1400 mm^2.

Falling hydrometeors larger than approximately 0.1 mm in maximum dimension (representing approximately 1/100 000th of the trigger cross-section) are detected as a broken beam. The MASC microprocessor electronics are designed to accept only very rapidly varying fluctuations in the detected emission. The goal is to filter out ambient light fluctuations associated with varying sunlight and shadows. The instrument works equally well under all natural lighting conditions, including darkness. The capture interval can be as fast as the hydrometeor interarrival times, or limited to a desired frequency. Here it was set to once per second in order to limit excessive flashes near ski resort employee dormitories.

The fallspeed is calculated from the time interval between two successive triggers, vertically separated by 32 mm, which allows only for a trajectory from the top to the bottom of the triggering arrays. The automated calculation is double checked for repeatability and accuracy in the laboratory. This is done by measuring the length of photographed motion blur of a small bead, captured at a slow camera shutter speed.

The MASC microprocessor controls the camera and communications via PC using a Firewire 800 Line for image data and one USB-RS232 Converter for camera control. The camera driver is supplied by Unibrain for use with Microsoft Windows. In-house software has been developed for data acquisition of images, fallspeeds, timestamps, and housekeeping variables.

3 Image analysis

Analysis of MASC images has been performed using the MATLAB image processing toolbox. Hydrometeors in MASC images occupy only a fraction of the picture frame. The region occupied by the hydrometeor is identified using a Sobel edge detection algorithm, which highlights regions of local gradients. The linear gradients in the frame are dilated by 200 µm (or the nearest pixel equivalent) both horizontally and vertically so that an enclosing area can be identified and filled. The area is then eroded horizontally and vertically by the same degree as the dilation. The result is a frame with pixels having a value of 1 for the hydrometeor location and 0 for the background.

Only frames containing a single hydrometeor are considered, provided that less than a linear length of 0.5 mm of the hydrometeor domain touches the frame edges, and that the maximum pixel brightness is at least 0.2 (or 51 on a scale of 0 to 255). Due to a mismatch between the depth of field for the motion sensor triggers and the depth of field for the camera images, images are normally out of focus.

For the sake of analysis, hydrometeor data is considered in post-analysis only if it passed a focus threshold. There is no foolproof method for automatically distinguishing out of focus images when the particle shapes are not known a priori and they are unpredictably complex. However, we found that out of focus images tend to be relatively dark and lacking in internal gradients. To identify such images, a map is calculated for the standard deviation of pixel brightness, based on a 3×3 neighborhood around each pixel within the hydrometeor domain. Images are rejected as being out of focus if the mean standard deviation for the hydrometeor domain is less than or equal to 0.02, or 5 on a scale of 0 to 255.

If at least two of the three camera images satisfy the above image acceptance criteria, then images are analyzed for a range of properties, averaged over camera perspectives. These properties include the average maximum dimension along the major axis D_{max}, the aspect ratio relative to the minimum dimension along the minor axis $\alpha = D_{\text{min}}/D_{\text{max}}$, the angle from the horizontal to the major axis θ, the hydrometeor

cross-section σ allowing for internal holes, the hydrometeor perimeter P, and a dimensionless expression of the hydrometeor complexity

$$\chi = \frac{P}{2\pi r_{eq}} \tag{2}$$

where the equivalent radius r_{eq} is the radius of an equivalent cross-section circle

5 $r_{eq} = \sqrt{\sigma/\pi} \tag{3}$

Thus $\chi = 1$ for a spherical particle, it is close to unity for quasi-spherical particles such as graupel, and it is larger for more complex aggregate shapes. A very crude estimate of hydrometeor mass takes advantage of the multiple camera perspectives

$$m = \frac{4}{3}\pi\rho \left\langle r_{eq} \right\rangle^3 \tag{4}$$

10 where ρ is the bulk density of liquid or ice. More sophisticated estimates would account for internal density (Judson and Doesken, 2000; Kajikawa et al., 2004), but this is not known based on MASC measurements alone.

4 Measurements

All measurements described here were obtained at an altitude of 2600 m at the base of
15 Collins Gulch, the uppermost side canyon in Little Cottonwood Canyon, located within the Wasatch Front about twenty miles south of Salt Lake City. The measurement site was outside the home of co-author DH, within the Alta Ski Area bounds. From the base of the ski area, Collins Gulch rises vertically through a depth of 760 m, to the summit of Mt. Baldy at 3350 m altitude. During storms, prevailing winds are normally up Little
20 Cottonwood Canyon, but Collins Gulch is relatively sheltered compared to the Mt. Baldy ridgeline.

No wind skirt was placed around the MASC, such as those commonly used in precipitation gauge systems. Wind skirts are designed to maximize the efficiency of the catch. However, it has recently been shown that they can also introduce hydrometeor size and shape selection biases (Thériault et al., 2012). Since a wind skirt was not used, what was measured was not necessarily the hydrometeor terminal velocity, but rather a hydrometeor settling speed representing a convolution of the terminal velocity within a turbulent wind field.

The data described here were collected between 10 February and 6 April in 2012. Approximately ten thousand images were obtained that satisfied the conservative rejection criteria outlined in Sect. 3. A small selection of images from the MASC are shown in Fig. 2, chosen to highlight the extraordinary range and complexity of forms that characterize frozen hydrometeors. Hexagonally symmetric forms were observed only very rarely.

From this dataset, Fig. 3 shows probability distributions for maximum dimension D_{max}, equivalent radius r_{eq}, aspect ratio α, orientation θ, complexity χ and fallspeed V. In all regards, the range of possible characteristics is broad. The atmosphere seems to allow for most possibilities. However, in general, the size and fallspeed measurements are broadly consistent with past measurements indicating typical linear dimensions of about 1 mm and fallspeeds of about $1\,\mathrm{m\,s^{-1}}$ (Barthazy and Schefold, 2006; Brandes et al., 2007, 2008; Gunn, 1967; Heymsfield and Westbrook, 2010; Magono and Nakamura, 1965; Mitchell et al., 1990; Yuter et al., 2006; Zawadzki et al., 2010). The hydrometeors that were observed tended to have low complexity, with a clear preference for a near unity aspect ratio. The maximum dimension tends to lie nearer the horizontal than the vertical, although a wide variety of orientations is possible (cf., Xie et al., 2012).

From the dataset that was obtained, Fig. 4 shows a time series of analyzed parameters from over a one week period beginning on 18 February, 2012. Mean values are calculated in 20 min blocks provided that there are at least 20 hydrometeors per block that satisfied the aforementioned thresholding criteria. What is notable from the data is

Full Screen / Esc

Printer-friendly Version

Interactive Discussion

that there are periods where there were abrupt changes in some hydrometeor characteristics but not others. For example, late on 21 Feburary, the images showed a mixture of graupel and rimed needles. At around 21:00 MST, the same mixture was observed, but the needles became highly aggregated. This abrupt change appears in the time series shown in Fig. 4 as markedly larger and more complex particles. However, there is no coincident transition in fallspeed.

Also, near midnight on 22 February, there was a graupel event, with large mean particle diameters ranging from 2 mm to 4 mm. Following a break in the storm, there was a transition to more aggregated shapes in the morning of 23 February. These particles were equally large, but more complex, slower falling, and with a smaller aspect ratio.

5 Microwave scattering calculations

MASC data may also be used to refine hydrometeor morophology used as input to microwave scattering calculations. Often, these calculations are done using the discrete dipole approximation method (DDA) (Draine and Flatau, 1994), where the hydrometeor is represented as a dielectric array of electromagnetic dipoles (Liu, 2008a). A popular code for calculating scattering properties is DDSCAT, developed by Draine and Flatau (2008).

DDSCAT calculations can be made for an arbitrary choice of dielectric media and dipole arrangements within the array. The trade-off of this flexibility is that the calculations can be computationally expensive. For sufficient accuracy, the theoretical requirement is that the dipole grid spacing d satisfies Eq. (1), such that $2\pi |n| d / \lambda < 0.5$, where n is the complex refractive index of the hydrometeor, and λ is the incident wavelength of the electromagnetic radiation. However, this might easily require over 50 GB of shared computer memory. As pointed out by Xie et al. (2012), it is normally not worth the expense of making discrete dipole approximation calculations unless a realistic representation of hydrometeor form can be ascertained. Here, the MASC provides a degree

of detail that has not previously been possible, perhaps making DDSCAT calculations worthwhile. To illustrate, triplet stereoscopic snowflake photographs from the MASC are shown in Fig. 5. For microwave scattering calculations (i.e., $\lambda = 2\pi/k > 1\,\mathrm{mm}$ and $|n| \sim 1.78$), the MASC resolution of $9\,\mu\mathrm{m}$ or $27\,\mu\mathrm{m}$ exceeds the degree of detail that

5 is required for making discrete dipole approximation calculations. Further, the MASC provides some representation of the three-dimensional structure of the hydrometeors because it provides an angular perspective spanning $72°$. Unfortunately, recreating a full three-dimensional hydrometeor structure remains out of reach, at least for hydrometeors A through C in Fig. 5. Their structure is much too complicated.

10 Nonetheless, a more approximate approach might be the following. The first step is to estimate the volume of the snowflakes from the average equivalent radius for the three projections

$$V = \frac{4}{3}\pi \langle r_{\mathrm{eq}} \rangle^3 \tag{5}$$

Second, for each image perspective, the photographed snowflake cross-section is ex-
15 truded normal to the cross-section plane a distance $V/(\pi r_{\mathrm{eq}}^2)$ until its volume is equal to V. For example, if the cross-section were a hexagonal plate, its extruded form would be a hexagonal column. Here, the shapes are more complicated, so the extruded form might include internal holes that extend through the depth of the extrusion. An example for hydrometeor B in Fig. 5 is shown in Fig. 6.

20 Third, for each of the three extruded forms, the scattering properties are calculated using DDSCAT, treating the form as an internal mixture of ice and air. The ice is given a refractive index specific to the wavelength of the incident radiation (Warren and Brandt, 2008). Finally, the calculated scattering properties are averaged across perspectives, weighted by the scattering cross-section calculated for each camera per-
25 spective.

Figure 7 shows calculations for the unpolarized angular scattering matrices (or phase functions) of each of the hydrometeors in Fig. 5, evaluated for an incident frequency of $183\,\mathrm{GHz}$, or a wavelength of $1.64\,\mathrm{mm}$. What stands out is that a graupel particle

has a much lower scattering efficiency Q_{sca}, and is more strongly biased towards back-scattering, than snow particles with a similar volume equivalent effective radius $a_{eff} = \left(3V/4\pi\right)^{1/3}$. The differences are particularly marked in the back-scattering regime that matters most to active microwave remote-sensing. A possible explanation is that the

5 components of aggregated ice particles can produce interference patterns that lead to preferential forward-scattering when their separation is small compared to the incident wavelength (Videen et al., 1998).

6 Conclusions

This paper has described a new instrument for taking automated, high-resolution,
10 stereoscopic photographs of hydrometeors in freefall while simultaneously measuring their fallspeed. The Multi-Angle Snowflake Camera (MASC) resolution is as fine as 9 µm, and the cameras are triggered by hydrometeors ranging from as small as 100 µm up to several centimeters. Three views of each hydrometeor from angles spanning 72° help to constrain estimates of particle size, shape and orientation. Fallspeeds are de-
15 termined from the time interval between triggers of two vertically separated arrays of infrared motion sensors.

The instrument has been designed to help improve representations of frozen hydrometeors in weather and remote sensing models. Weather model forecasts are sensitive to the details of bulk microphysical parameterizations for hydrometeor form and
20 fallspeed. Remote sensing algorithms, particularly those using active and passive signals in the microwave, rest on assumed relationships between the mass of a hydrometeor and its scattering cross-section.

Between February and April 2012, continuous measurements were obtained with the MASC at an altitude of 2600 m, in the Wasatch Front near Salt Lake City, UT. This paper
25 has shown time series and statistical distributions collected during this period for such parameters as particle fallspeed, size, orientation, aspect ratio and a dimensionless measure of complexity. For each of these parameters, a very broad range of values

Hydrometeor fallspeed and multi-angle photography

T. J. Garrett et al.

|◄ | ►|

◄ | ►

Back | Close

Full Screen / Esc

Printer-friendly Version

Interactive Discussion

was measured, although we observed a bias towards rounder shapes with an aspect ratio near unity, sizes of about 1 mm, and fallspeeds of approximately $1 \, \mathrm{m \, s^{-1}}$.

We also show an example of how the high-resolution multi-angle capabilities of the MASC might be used to help constrain discrete dipole approximation computations of the microwave scattering phase function for hydrometeors (Draine and Flatau, 2008). While preliminary, these calculations highlighted the importance of the small-scale details of hydrometeors to their scattering properties. We found that for particles with a size similar to the microwave wavelength, and with nearly equivalent estimated mass, graupel appears to be more weakly back-scattering and more strongly forward scattering than lossely aggregated snowflake shapes.

References

Barthazy, E. and Schefold, R.: Fall velocity of snowflakes of different riming degree and crystal types, Atmos. Res., 82, 391–398, 2006. 4829, 4835

Barthazy, E., Göke, S., Schefold, R., and Högl, D.: An optical array instrument for shape and fall velocity measurements of hydrometeors, J. Atmos. Ocean. Tech., 21, 1400–1416, doi:10.1175/1520-0426(2004)021<1400:AOAIFS>2.0.CO;2, 2004. 4829

Brandes, E. A., Ikeda, K., Zhang, G., Schönhuber, M., and Rasmussen, R. M.: A statistical and physical description of hydrometeor distributions in Colorado snowstorms using a video disdrometer, J. Appl. Meteorol. Clim., 46, 634–650, doi:10.1175/JAM2489.1, 2007. 4835

Brandes, E. A., Ikeda, K., Thompson, G., and Schönhuber, M.: Aggregate terminal velocity/temperature relations, J. Appl. Meteorol. Clim., 47, 2729–2736, doi:10.1175/2008JAMC1869.1, 2008. 4835

Bruintjes, R. T., Heymsfield, A. J., and Krauss, T. W.: An examination of double-plate ice crystals and the initiation of precipitation in continental cumulus clouds, J. Atmos. Sci., 44, 1331–1349, 1987. 4829

Title Page

Abstract | Introduction

Conclusions | References

Tables | Figures

◄ | ►

◄ | ►

Back | Close

Full Screen / Esc

Printer-friendly Version

Interactive Discussion

Colle, B. A., Garvert, M. F., Wolfe, J. B., Mass, C. F., and Woods, C. P.: The 13 14 December 2001 IMPROVE-2 Event. Part 3: Simulated microphysical budgets and sensitivity studies., J. Atmos. Sci., 62, 3535–3558, doi:10.1175/JAS3552.1, 2005. 4828, 4829

Draine, B. T. and Flatau, P. J.: Discrete-dipole approximation for scattering calculations, J. Opt. Soc. Amer., 11, 1491–1499, 1994. 4836

Draine, B. T. and Flatau, P. J.: User guide for the Discrete Dipole Approximation Code DDSCAT 7.0, arXiv, available at: http://arxiv.org/abs/0809.0337v4 (last access: June 2012), 2008. 4829, 4836, 4839

Garvert, M. F., Woods, C. P., Colle, B. A., Mass, C. F., Hobbs, P. V., Stoelinga, M. T., and Wolfe, J. B.: The 13 14 December 2001 IMPROVE-2 Event. Part 2: Comparisons of MM5 model simulations of clouds and precipitation with observations., J. Atmos. Sci., 62, 3520–3534, doi:10.1175/JAS3551.1, 2005. 4828

Gunn, K. L. S.: The number flux of snow crystals at the ground, Mon. Wea. Rev., 95, 921–924, doi:10.1175/1520-0493(1967)095<0921:TNFOSC>2.3.CO;2, 1967. 4835

Heymsfield, A. J. and Westbrook, C. D.: Advances in the estimation of ice particle fall speeds using laboratory and field measurements, J. Atmos. Sci., 67, 2469–2482, doi:10.1175/2010JAS3379.1, 2010. 4835

Ishimoto, H.: Radar backscattering computations for fractal-shaped snowflakes, J. Met. Soc. Jpn., 86, 459–469, 2008. 4829

Judson, A. and Doesken, N.: Density of freshly fallen snow in the Central Rocky Mountains., B. Am. Meteorol. Soc., 81, 1577–1588, 2000. 4834

Kajikawa, M., Goto, H., Kanaya, K., and Kikuchi, K.: Multiple regression equations for the estimation of new snow density from meteorological elements, J. Jap. Soc. Snow and Ice, 66, 561–565, 2004. 4834

Kruger, A. and Krajewski, W. F.: Two-dimensional video disdrometer: a description, J. Atmos. Ocean. Tech., 19, 602–617, 2002. 4829

Lin, Y., Farley, R. D., and Orville, H. D.: Bulk parameterization of the snow field in a cloud model., J. Appl. Meteorol., 22, 1065–1092, doi:10.1175/1520-0450(1983)022<1065:BPOTSF>2.0.CO;2, 1983. 4828

Liu, G.: A database of microwave single-scattering properties for nonspherical ice particles, B. Am. Meteorol. Soc., 89, 1563–1570, 2008a. 4836

Liu, G.: Deriving snow cloud characteristics from CloudSat observations, J. Geophys. Res., 113, D00A09, doi:10.1029/2007JD009766, 2008b. 4828

Hydrometeor fallspeed and multi-angle photography

T. J. Garrett et al.

Title Page

Abstract	Introduction
Conclusions	References
Tables	Figures

Back | Close

Full Screen / Esc

Printer-friendly Version

Interactive Discussion

Locatelli, J. D. and Hobbs, P. V.: Fall speeds and masses of solid precipitation particles, J. Geophys. Res., 79, 2185–2197, doi:10.1029/JC079i015p02185, 1974. 4829

Magono, C. and Nakamura, T.: Aerodynamic studies of falling snowflakes, J. Meteor. Soc. Japan., 43, 139–147, 1965. 4835

Maruyama, K.-I. and Fujiyoshi, Y.: Monte Carlo simulation of the formation of snowflakes., J. Atmos. Sci., 62, 1529–1544, doi:10.1175/JAS3416.1, 2005. 4829

Matrosov, S.: Modeling backscatter properties of snowfall at millimeter wavelengths, J. Atmos. Sci., 64, 1727–1736, doi:10.1175/JAS3904.1, 2007. 4828

Milbrandt, J. A., Yau, M. K., Mailhot, J., Bélair, S., and McTaggart-Cowan, R.: Simulation of an orographic precipitation event during IMPROVE-2. Part 2: Sensitivity to the number of moments in the bulk microphysics scheme, Mon. Weather Rev., 138, 625–642, doi:10.1175/2009MWR3121.1, 2010. 4828

Mitchell, D. L., Zhang, R., and Pitter, R. L.: Mass-dimensional relationships for ice particles and the influence of riming on snowfall rates., J. Appl. Meteorol., 29, 153–164, doi:10.1175/1520-0450(1990)029<0153:MDRFIP>2.0.CO;2, 1990. 4829, 4835

Newman, A. J., Kucera, P. A., and Bliven, L. F.: Presenting the snowflake video imager (SVI), J. Atmos. Ocean. Tech., 26, 167–179, doi:10.1175/2008JTECHA1148.1, 2009. 4829

Noh, Y.-J., Liu, G., Jones, A. S., and Vonder Haar, T. H.: Toward snowfall retrieval over land by combining satellite and in situ measurements, J. Geophys. Res., 114, D25205, doi:10.1029/2009JD012307, 2009. 4828

Nowell, H. K.: Modeling snow aggregates and their single-scattering properties: Implications to snowfall remote sensing, Master's thesis, Florida State University, Tallahassee, Florida, available at: http://diginole.lib.fsu.edu/etd/2511/ (last access: June 2012), 2010. 4829

Oguchi, T.: Electromagnetic wave propagation and scattering in rain and other hydrometeors, P. IEEE, 71, 1029–1078, doi:10.1109/PROC.1983.12724, 1983. 4829

Reisner, J., Rasmussen, R. M., and Bruintjes, R. T.: Explicit forecasting of supercooled liquid water in winter storms using the MM5 mesoscale model, Q. J. Roy. Meteorol. Soc., 124, 1071–1107, doi:10.1256/smsqj.54803, 1998. 4828

Rutledge, S. A. and Hobbs, P. V.: The mesoscale and microscale structure and organization of clouds and precipitation in midlatitude cyclones. XII: a diagnostic modeling study of precipitation development in narrow cold-frontal rainbands., J. Atmos. Sci., 41, 2949–2972, doi:10.1175/1520-0469(1984)041<2949:TMAMSA>2.0.CO;2, 1984. 4828

Hydrometeor fallspeed and multi-angle photography

T. J. Garrett et al.

Title Page

Abstract	Introduction
Conclusions	References
Tables	Figures

◄◄ ►►

◄ ►

Back Close

Full Screen / Esc

Printer-friendly Version

Interactive Discussion

Skofronick-Jackson, G. M., Kim, M.-J., Wieinman, J. A., and Chang, D.-E.: A physical model to determine snowfall over land by microwave radiometry, IEEE T. Geosci. Remote, 42, 1047–1058, 2004. 4828

Thériault, J. M., Rasmussen, R., Ikeda, K., and Landolt, S.: Dependence of snow gauge collection efficiency on snowflake characteristics, J. Appl. Meteor. Clim., 51, 745–762, doi:10.1175/JAMC-D-11-0116.1, 2012. 4829, 4835

Videen, G., Pinnick, R. G., Ngo, D., Fu, Q., and Chýlek, P.: Asymmetry parameter and aggregate particles, Appl. Optics, 37, 1104–1109, 1998. 4838

Warren, S. G. and Brandt, R. E.: Optical constants of ice from the ultraviolet to the microwave: a revised compilation, J. Geophys. Res., 113, D14220, doi:10.1029/2007JD009744, 2008. 4837

Westbrook, C. D., Ball, R. C., and Field, P. R.: Radar scattering by aggregate snowflakes, Q. J. Roy. Meteorol. Soc., 132, 897–914, 2006. 4829

Xie, X., Löhnert, U., Kneifel, S., and Crewell, S. L.: Snow particle orientation observed by ground-based microwave radiometry, J. Geophys. Res., 117, D02206, doi:10.1029/2011JD016369, 2012. 4835, 4836

Yuter, S. E., Kingsmill, D. E., Nance, L. B., and Löffler-Mang, M.: Observations of precipitation size and fall speed characteristics within coexisting rain and wet snow, J. Appl. Meteorol. Clim., 45, 1450–1464, doi:10.1175/JAM2406.1, 2006. 4829, 4835

Zawadzki, I., Jung, E., and Lee, G.: Snow studies. Part 1: A study of natural variability of snow terminal velocity, J. Atmos. Sci., 67, 1591–1604, doi:10.1175/2010JAS3342.1, 2010. 4829, 4835

Title Page

Abstract | Introduction

Conclusions | References

Tables | Figures

◀ | ▶

◀ | ▶

Back | Close

Full Screen / Esc

Printer-friendly Version

Interactive Discussion

Table 1. Lens and camera parameters for the Multi-Angle Snowflake Camera.

Camera lens/body	Horizontal Field of View (mm)	Depth of Field at f/5.6 (mm)	Image resolution (μm)
12 mm/1.2 MP	47	15	36
16 mm/1.2 MP	35	10	27
35 mm/5 MP	22	2	9
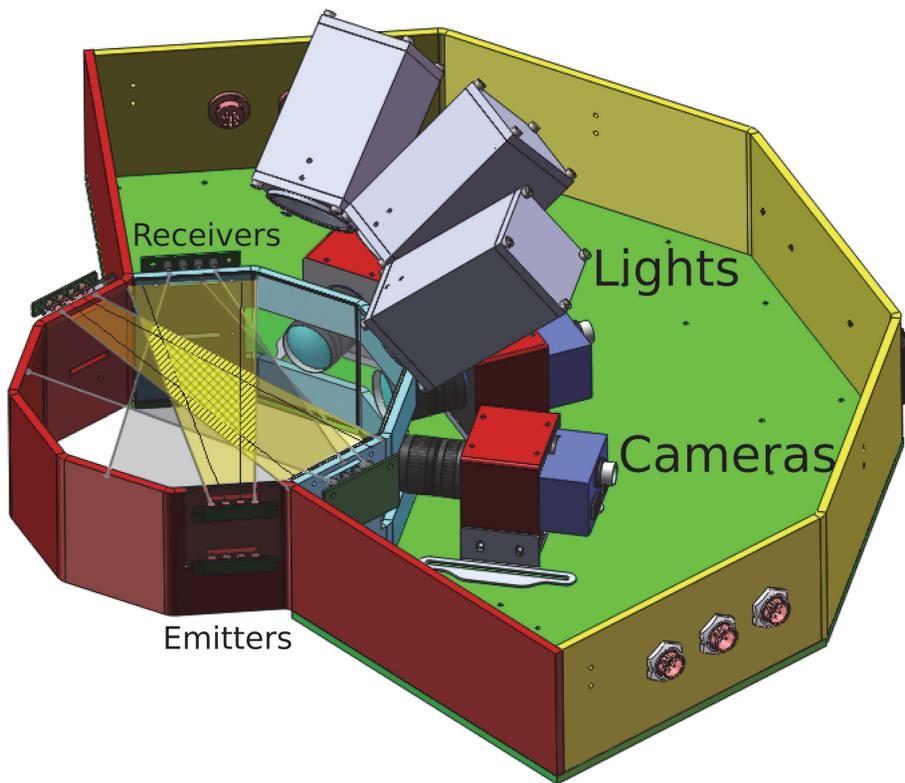
Fig. 1. Schematic of the basic components of the Multi-Angle Snowflake Camera. The hatched region represents the cross-section for triggering of the near-infrared motion detector system.

Title Page

Abstract | Introduction

Conclusions | References

Tables | Figures

◄ | ►►

◄ | ►

Back | Close

Full Screen / Esc

Printer-friendly Version

Interactive Discussion

5 mm
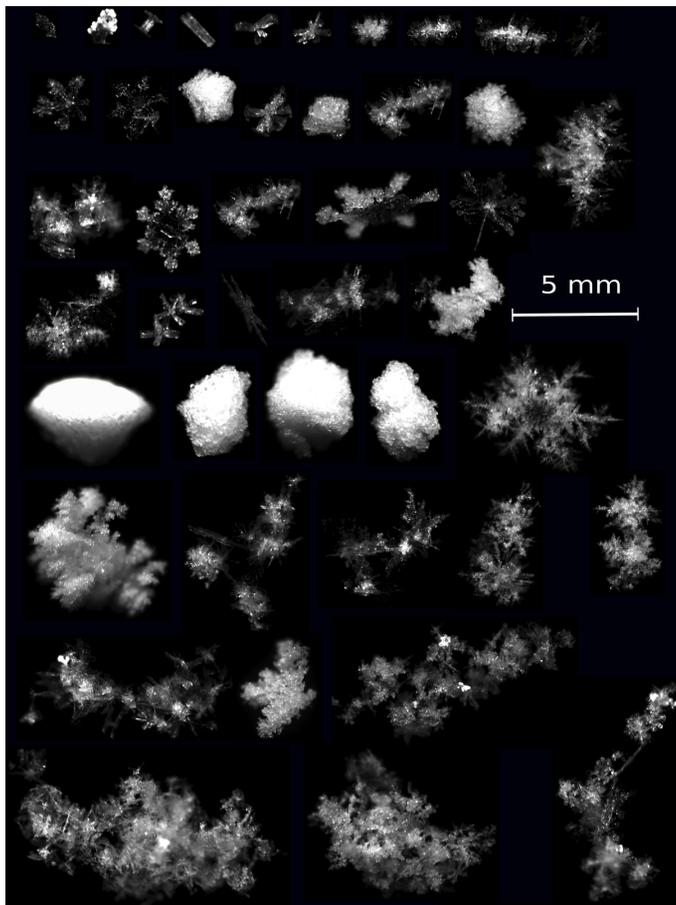
Fig. 2. A sample of MASC images of hydrometeors in freefall taken using a 35 mm lens on a 5 MP camera.
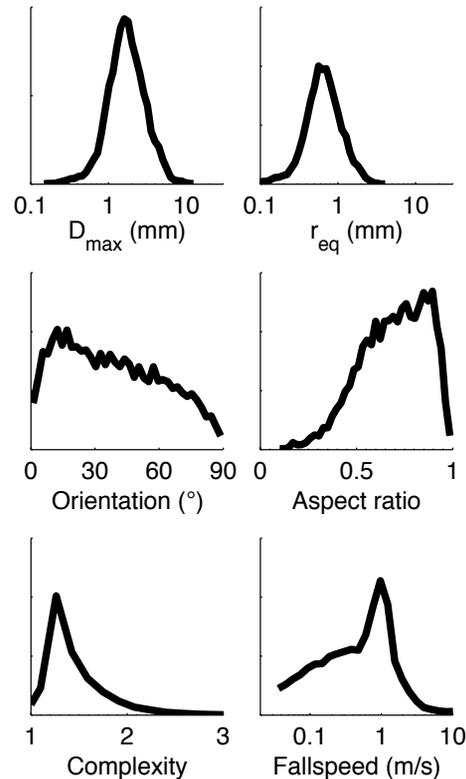
Fig. 3. MASC statistics based on approximately 10 000 images obtained at Alta Ski Area. The dimensionless representation of hydrometeor complexity is defined by the ratio of the hydrometeor perimeter to its equivalent cross-section circumference. For example, the complexity value is unity for a droplet.
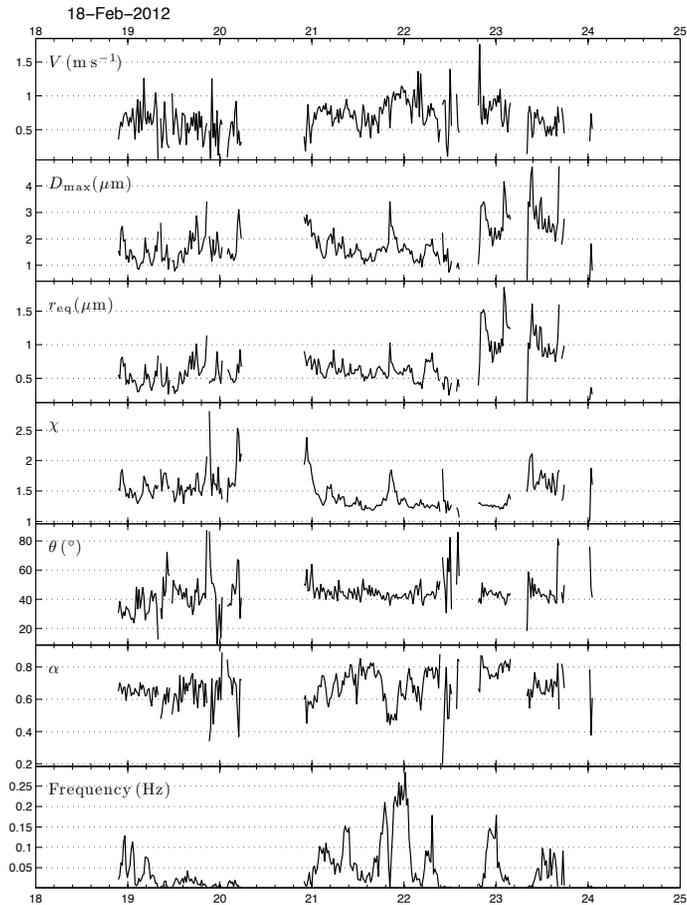
Fig. 4. A time series of analyzed parameters from MASC photography and fallspeed data over a one week period beginning 18 February 2012. The time stamp is in MST.
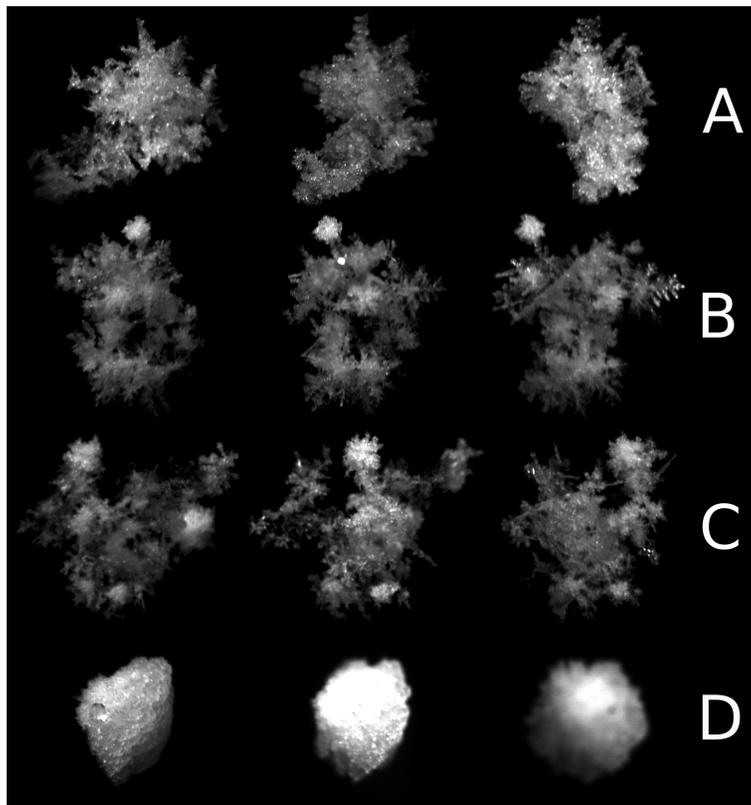
Fig. 5. Triplet stereoscopic images of individual snowflakes imaged with the MASC. The center resolution is 9 µm and outside image resolution is 27 µm.
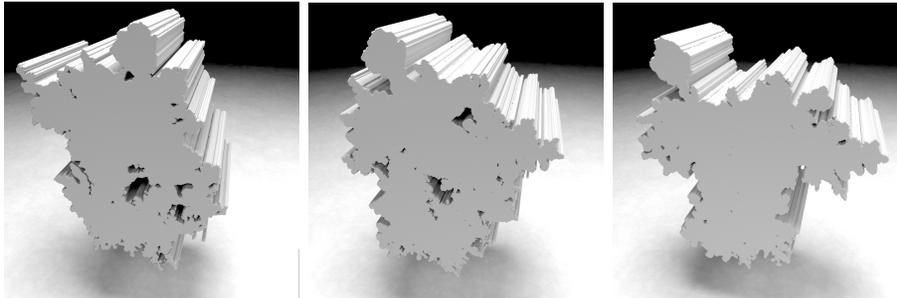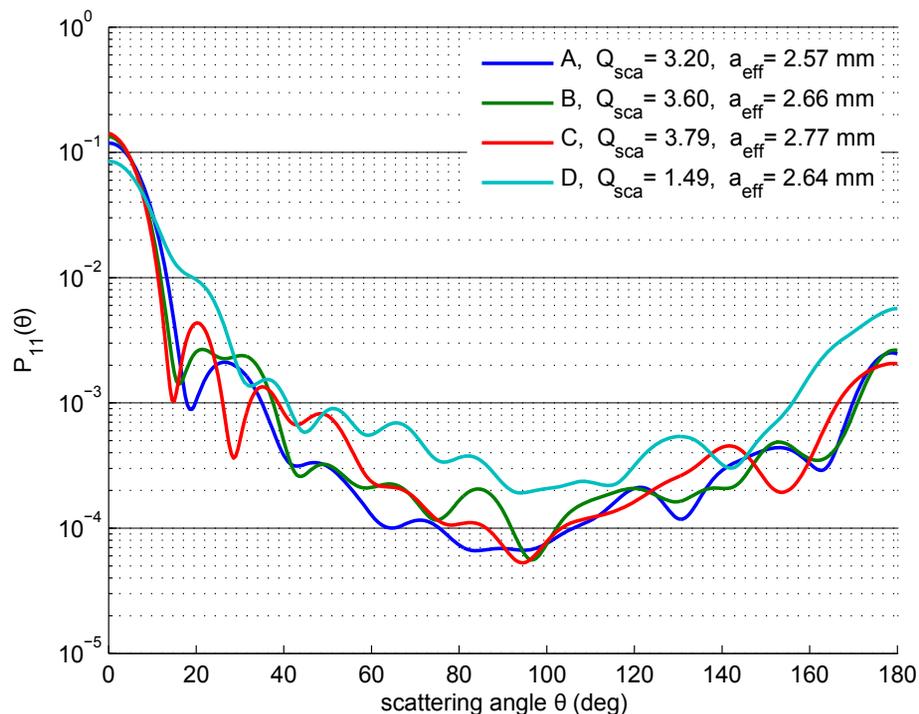
Fig. 6. Example of the triplet form for an extruded ice flake used for input to DDSCAT (hydrometeor B in Fig. 5). Displays are rendered with Monte Carlo ray tracing, based on idealized surface material properties, using a Metropolis sampling method.

Fig. 7. DDA phase function calculations for the hydrometeors shown in Fig. 5, assuming a mesh of ice and a vacuum for 1.64 mm wavelength (183 GHz) incident radiation.